PAPER

Check for updates

Electrochemically embedded heterostructured Ni/NiS anchored onto carbon paper as bifunctional electrocatalysts for urea oxidation and hydrogen evolution reaction†

Saba A. Aladeemy, Prabhakarn Arunachalam, [ID] * Mabrook S. Amer [ID] and Abdullah M. Al-Mayouf [ID] *

Developing high-efficiency, cost-effective, and long-term stable nanostructured catalysts for electrocatalytic water splitting remains one of the most challenging aspects of hydrogen fuel production. Urea electrooxidation reaction (UOR) can produce hydrogen energy from nitrogen-rich wastewater, making it a more sustainable and cheaper source of hydrogen. In this study, we have developed Ni/NiS hybrid structures with cauliflower-like morphology on carbon paper electrodes through the application of dimethylsulfoxide solvents. These electrodes serve as highly efficient and long-lasting electrocatalysts for the hydrogen evolution reactions (HER) and UOR. In particular, the Ni/NiS cauliflower-like morphology is confirmed *via* X-ray photoelectron spectroscopy (XPS) and scanning electron microscopy (SEM). Furthermore, electrochemical characterization of the Ni/NiS@CP catalyst showed a 1.35 V onset potential *versus* RHE for the UOR in 1.0 M KOH and superior electrocatalytic performance compared to bare Ni@CP. Additionally, the Ni/NiS@CP catalyst also exhibits a low overpotential of 125 mV at 10 mA cm^{-2} for HER in 0.5 M H$_2$SO$_4$ with excellent durability, which is apparently lower than bare Ni@/CP (397 mV). Based on the results obtained, the synthesized Ni/NiS@CP catalyst may be a promising electrode candidate for handling urea-rich wastewater and generating hydrogen.

1 Introduction

Increasing economic and human prosperity needs have led to a tremendous increase in global energy crises. To meet energy needs and reduce environmental concerns, clean energy sources and technologies must be developed. Consequently, hydrogen has a low carbon content and high energy density, making it a potential replacement for fossil fuels.[1,2] Sustainable and clean energy is generated by electrochemical processes involving water and organic molecules.[3–5] In electrocatalytic water splitting, there are two redox half-reactions occurring simultaneously: HER and OER (oxygen evolution reaction). Since the OER has a slow kinetics and a high theoretical voltage (1.23 V *vs.* RHE), it is viewed as a bottleneck for hydrogen economy and electrochemical energy production.[1,2,6] Due to these limitations, it is necessary to find a versatile alternative for OER,[7–9] such as the urea electrolysis reaction (UOR), which generates hydrogen at a much lower theoretical voltage (0.37 V) than water splitting.[10–12] As a renewable energy source, urea has

ideal energy density (16.9 MJ L^{-1}),[5,7] as well as its non-toxicity, non-flammability, availability, non-volatility, storage stability, and renewable properties.[13,14] The decomposition of urea naturally releases products toxic ammonia (NH$_3$) and nitrate (NO$_3^-$), increasing environmental pollution and health concerns, whereas the alkaline UOR leads to harmless products of (CO$_3^{2-}$) and nitrogen (N$_2$): CO(NH$_2$)$_2$ + 6OH$^-$ → N$_2$ + 5H$_2$O + CO$_2$ + 6e$^-$.[7,8] The deployment of noble metallic electrocatalysts (pt, Ir, Ru) has been substantially constrained by their limited global geological reserves and prohibitively elevated economic procurement and implementation expenses.[4,15,16] In order to accomplish this, it is urgently required to develop enhanced and cost-effective bifunctional catalysts for both UOR and HER.

In recent years, transition metal chalcogenides (*e.g.* sulfide) nanocatalysts have recently been recommended as more preferable electrocatalysts for HER, OER, and alkaline UOR.[17–19] It has been shown that various nickel sulfides (Ni$_x$S$_y$) are more electrochemically active in acidic and alkaline conditions than their oxide counterparts due to their ability to control their electronic structure. Various electrocatalysts have been constructed by strategically integrating high-density catalytically active sites and structural defects with lattice distortions, a multifunctional catalytic architecture is engineered to enhance catalytic performance and versatility.[1,2]

Electrochemical Sciences Research Chair (ESRC), Chemistry Department, King Saud University, P.O Box 2455, Riyadh 11451, Saudi Arabia. E-mail: parunachalam@ksu.edu.sa; amayouf@ksu.edu.sa

† Electronic supplementary information (ESI) available. See DOI: https://doi.org/10.1039/d4ra07418a

Conventionally, Ni_xS_y nanostructured catalysts have been synthesized utilizing hydrothermal or solvothermal synthetic methodologies, employing nickel foam as the primary substrate and structural support. Moreover, Ni_xS_y catalysts for HER and UOR can be readily reconstructed by facile electrodeposition from aqueous solutions.[20–22] An additional point to be noted is that some Ni_xS_y phases (such as α-NiS, β-NiS, NiS_2, Ni_7S_6, Ni_3S_2, and Ni_9S_8) can enhance the structure and composition tuning more effectively to suit a given catalytic reaction. As an example, Tian et al.[23] have developed a metal–organic framework-embedded microwave sulfurization method for pyrite-type NiS_2 microspheres. Similarly, Ren et al.[24] fabricated bifunctional Ni_3S_2 films on Ni foam by directly depositing mercaptoethanol solution, followed by thermal annealing at 300 °C. In a recent study, Wu et al.[25] successfully prepared nanoflower nano-NiS catalyst by hydrothermal method. Similarly, Li et al.[26] have developed hierarchically 3D-heteropore di-functional MoS_2/Ni_3S_2 catalysts for urea splitting. Additionally, it delivers 646 mA cm^{-2} (vs. RHE) from the heteropore MoS_2/Ni_3S_2 over 20 hours of operation. Liu et al.[27] have grown Ni_3S_2 nanowires directly on NF and employed them as a dual-functional catalysts for urea electrolysis in 1.0 M NaOH and 0.33 M urea. Liu et al.[28] fabricated N-doped NiS/NiS_2 (N-NiS/NiS_2) materials through low-temperature calcination and used them as trifunctional catalysts for UOR, HER, and OER. In addition, most Ni_xS_y materials with superior electronic conductivity and durability have been demonstrated for HER and OER reactions.[29,30] However, few recently published works utilized these catalysts as electrocatalysts for UOR in alkaline solution.[25,27,28] Moreover, early studies have combined carbon materials with Ni as an electrocatalyst to achieve UORs. Using a hydrothermal approach, Plascencia et al.[31] developed the first highly active carbon-supported Ni electrocatalyst. CP is favored for this reaction because of its key properties, including electrochemistry, porous structure, and electrical conductivity.[32] However, their reconstructions by potentiodynamic deposition from an organic dimethylsulfoxide solvent (DMSO) using CP support for UOR have not been investigated yet. Thus, further research is needed to explore the potential of these catalysts for UOR in alkaline solutions.

Herein, and, for the first time, a series of various Ni_xS/CP electrodes were successfully prepared via single-step electrodeposition using nickel chloride and thiourea as precursors for nickel and sulfur, in addition to DMSO as complexing agent and solvent for alkaline UOR and HER in acidic conditions on CP substrates. In both UOR and HER, Ni/Ni_xS@CP exhibits excellent catalytic features, requiring a working potential of 1.75 V to achieve a current density of 100 mA cm^{-2} for UOR and an overpotential of 376 mV for HER. A variety of physicochemical and electrochemical methods have been used to investigate the composition and morphology of surfaces. Consequently, this research presents a pragmatic and precisely modulated approach for synthesizing Ni_xS-derived electrocatalysts with potential scalable applications in nitrogen-laden effluent remediation and hydrogen generation within industrial process engineering frameworks.

2 Experimental section

2.1. Materials

Anhydrous nickel chloride ($NiCl_2$, 99.0%) was acquired from Alfa Aesar. We acquired urea from AVONCHEM Corp. and DMSO (99.0%) and thiourea from LOBA Chemie. For the working electrode, CP substrate was used (SIGRACETR, grade GDL-24BC, SGL Technologies). We obtained potassium hydroxide pellets (KOH, 85%) from AnalaR group. We used Milli-Q ultrapure water purification systems (18 MΩ resistivity) to purify the deionized water (DI). We used all chemicals without further purification.

2.2. Electrodeposition of Ni/NiS nanostructured catalysts on CP support

Within a sealed three-electrode electrochemical configuration, the Ni_xS cauliflower-morphology catalyst was synthesized via potentiodynamic electrodeposition methodology. In the conventional three-electrode cell, commercial CP was applied as the working electrode, Ag/AgCl (3.0 M KCl) was used as the reference electrode, and blank CP was engaged as the counter electrode. For a typical procedure, the electrode was immersed in a 50 mL solution of non-aqueous DMSO, containing different concentrations of anhydrous $NiCl_2$ (0.020, 0.035, 0.045, and 0.065 M), as well as 0.5 M thiourea. In the deposition solution, nitrogen bubbled incessantly for at least 30 minutes before electrodeposition and throughout the deposition procedure. The electrodeposition process was executed via cyclic voltammetry (CV) within a potential of successive linear sweeps between −1.25 and 0.2 V vs. Ag/AgCl at a sweep rate of 5 mV s^{-1} for 10 cycles at a reaction temperature at 60 °C to attain the Ni_xS nanostructured anchored CP, which were labeled as $Ni_{0.020}S$/CP, $Ni_{0.035}S$/CP, $Ni_{0.045}S$/CP, and $Ni_{0.065}S$/CP, respectively. After electrodeposition, Ni_xS/CP electrodes were gently rinsed with DI water after being removed from the deposition bath. The Ni_xS/CP were stored overnight at room temperature and annealed at 350 °C for 30 minutes in N_2 atmosphere, with 5 °C min^{-1} heating and cooling. During electrochemical measurements, Ni_xS/CP films were always kept under vacuum at room temperature. For comparison, the bare nickel film (Ni@CP) was also electrodeposited under the same condition. The mass loading of the as-made catalysts: $Ni_{0.020}S$/CP (Ni/NiS-1@CP), $Ni_{0.035}S$/CP (Ni/NiS-2@CP), $Ni_{0.045}S$/CP (Ni/NiS-3@CP), $Ni_{0.065}S$/CP (Ni/NiS-4@CP) and $Ni_{0.045}$/CP (Ni@CP) was quantified through gravimetric analysis, determining the differential mass before and after electrodeposition, yielding specific loadings of 0.6, 1.5, 1.75, 2.05, and 0.75 mg cm^{-2}, respectively.

2.3. Characterization

Powdered X-ray diffraction (XRD) data were collected via MiniFlex-600 (Rigaku) under Cu Kα irradiation (40 KV, 15 mA) to investigate crystallographic information and crystal structure of the as-deposited catalyst. FE-SEM images were logged on a JSM-7610F operating at 15 kV armed with a EDX analyzer to identify catalyst morphology. A JEOL 2100F microscope (Japan) with 200 kV operation was applied to conduct a high-resolution
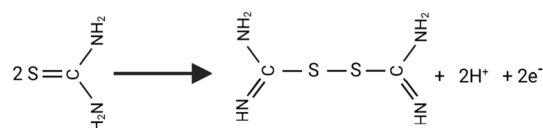
transmission microscope analysis (HR-TEM). An Escalab 250 spectrometer (Thermo-Fisher Scientific) was used to perform X-ray photoemission spectra analysis (XPS) on the surface. CV and chronoamperometry (CA) electrochemical measurements were conducted using autolabIII/FRA2 potentiostat/galvanostats controlled by NOVA1.11 software directly connected to a classical three-electrode electrochemical cell. During the UOR test, three electrode systems were employed: a working electrode (1.0 cm^2), a counter electrode (CP), and an Ag/AgCl reference electrode to deposit catalysts on a CP substrate's conductivity side. Electrolytes for UOR and HER were 1.0 M KOH in 0.33 M urea and 0.5 M H$_2$SO$_4$ respectively.

3   Results and discussion

3.1.   Catalyst characterization

Using a potentiodynamic deposition approach, Ni/NiS-decorated CP catalytic materials with a cauliflower-like structure were prepared with DMSO solution of anyhydrous NiCl$_2$ and thiourea. Fig. 1 shows the preparation process for Ni$_x$S catalytic materials on CP. The structured Ni$_x$S active materials were synthesized on carbon paper *via* a singular co-electrodeposition methodology, employing systematic variation of linear potential scanning and electrolyte composition, utilizing anhydrous NiCl$_2$ concentrations of 0.020, 0.035, and 0.065 M, with a constant 0.5 M thiourea concentration in DMSO under N$_2$ atmosphere. Fig. S1† illustrates the typical consecutive linear scans in the potential range between +0.2 to −1.25 V at a slow scan rate of 5.0 mV s^{-1} for the direct growth of hybrid Ni/NiS on CP at 60 °C using 0.065 M NiCl$_2$ and 0.5 M thiourea as precursors for Ni and S respectively, in addition to DMSO as the complexing agent and solvent. Accordingly, the observed peaks are due to the reduction of thiourea after its one-electron

oxidation to formamidine disulfide,[33] and its corresponding equation follows.

$$2\,S=C\begin{subarray}{l}NH_2\\ \\ H_2N\end{subarray} \longrightarrow \begin{subarray}{l}NH_2\\ \\ HN\end{subarray}C-S-S-C\begin{subarray}{l}NH_2\\ \\ HN\end{subarray} + 2H^+ + 2e^-$$

H$_2$S can be released at elevated temperatures due to thiourea decomposition, which further reacts with NiCl$_2$ complex to produce the NiS nucleus.[25] Moreover, during repeated cycling, the peak current increases with cycling and with increasing the nickel amount for various ratios of Ni$_x$S films. Notably, the color of the exposed area of CP turns into faint yellow from black after several cycles. Various Ni/Ni$_x$S/CP composite films were electrodeposited on carbon paper through precisely controlled potentiodynamic cyclic voltammetry, with an optimized deposition protocol of 10 cycles, resulting in systematically labeled specimens: Ni/NiS-1@CP, Ni/NiS-2@CP, and Ni/NiS-3@CP.

The XRD pattern was probed to investigate the crystal structure of a sequence of different as-synthesized Ni/NiS samples grown on CP substrate, as well, Ni film (Fig. 2a). Clearly, NiS (JCPDS No. 02-1280) diffraction peaks can be seen after template assisted electrodeposition reaction (shown as Ni/NiS-time). The comprehensive sulfidation of nickel is constrained by fundamental parametric variables including deposition duration, thermal conditions, and sulfur precursor concentration, thereby rendering the structural transformation process modifiable. Concomitantly, during NiS formation, XRD reveals characteristic crystallographic peaks corresponding to both Ni and NiS phases. The enlarged diffraction pattern of the Ni/NiS@CP samples in Fig. 2b matches the diffraction lines of Ni and NiS (JCPDS No. 02-1280). Sulfurization did not give rise to any other XRD peaks, indicating that no crystalline phase
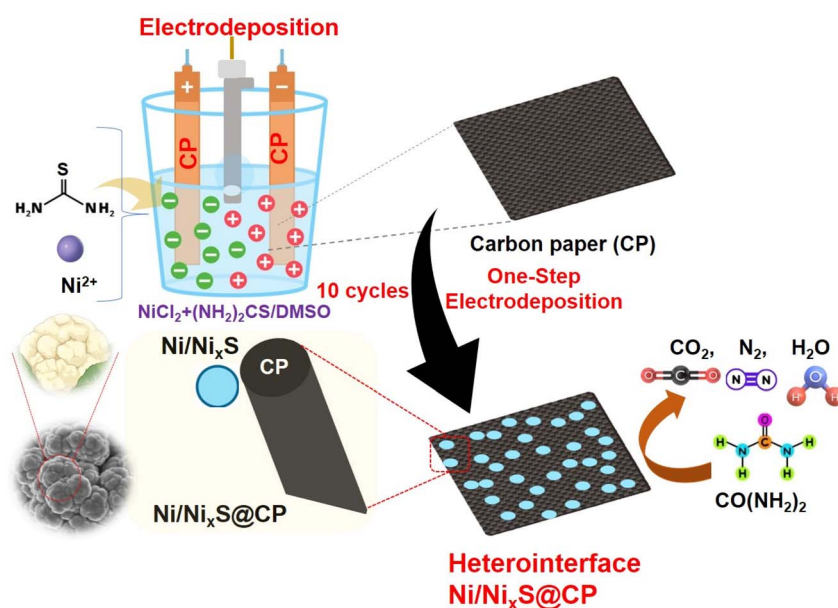

Fig. 1   A schematic illustration of the electrodeposition methods for Ni/Ni$_x$S films on CP substrates.
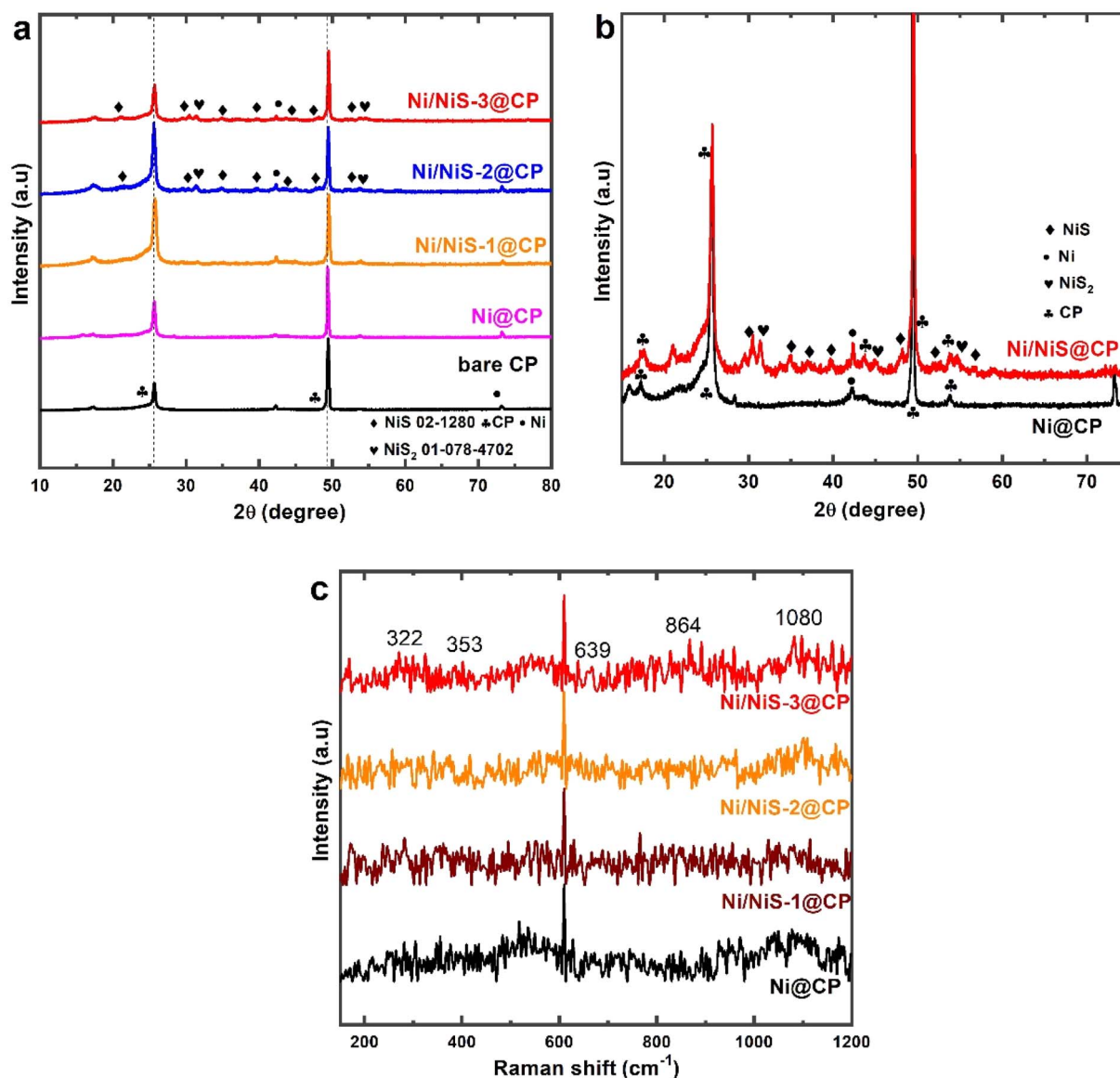
Paper

Fig. 2 (a) X-ray diffraction patterns of Ni@CP and different Ni/NiS@CP samples prepared by single-step electrodeposition process, (b) enlarged diffraction pattern and (c) Raman spectra of Ni and different Ni/NiS electrode materials.

emerged. The XRD pattern indeed shows both NiS and NiS_2 phases. However, upon further analysis and peak intensity comparison, it is evident that the NiS phase is dominant in our samples. In our samples, the predominant phase is NiS, while NiS_2 is the minority phase. Additionally, Fig. 2c shows Raman spectra of different deposited Ni/Ni_xS catalysts. The weak vibrational bands (322.4 and 353.7 cm^{-1}) might be caused by Ni/Ni_xS catalysts.[34,35] However, it is difficult to observe Raman peaks characteristic of Ni_xS in Ni/Ni_xS@CP heterostructures because of the small Ni_xS volume.[34,35] Due to Ni_xS's low volume, heterostructures have weak signal intensities, making peaks difficult to distinguish from background noises. In addition, the Raman peaks were also observed at higher wavenumbers (639, 864, and 1080 cm^{-1}), associated with the CP substrate bands.

The structure morphology of the as-deposited Ni/NiS samples was probed by FE-SEM. As shown in Fig. 3, FE-SEM images of bare CP electrodes were taken before and after the electrodeposition of Ni/NiS hybrid nanostructures prepared with different concentrations of anhydrous $NiCl_2$ and thiourea in DMSO solution. As shown in the results, the CP consisted of aggregated carbon nanoparticles with a particle size of 70–100 nm. In addition, the CP substrate features a mesoporous structure between nanoscale particle structures, enhancing diffusive transport and promoting interfacial catalysis (Fig. 3a). After electrodeposition of nickel from a non-aqueous electrolytic medium, the CP was fully enveloped by the nickel nanoparticles electrocatalyst layer, as illustrated in Fig. 3b. Obviously, after electrodeposition of Ni_xS, the microstructure morphology of the hybrid catalyst mainly reveals a uniform
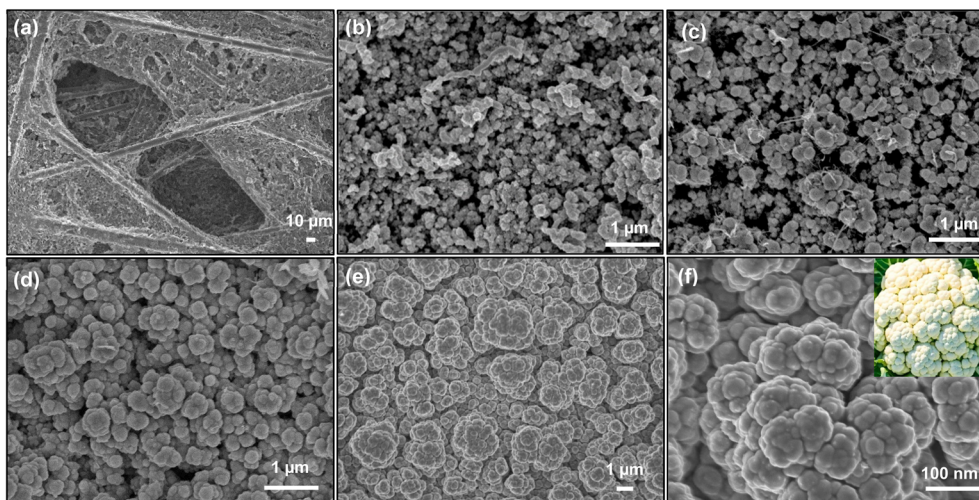
Fig. 3 Morphological characterizations. FE-SEM photographs of (a) CP substrate, (b) Ni@CP, (c) Ni/NiS-1@CP, (d) Ni/NiS-2@CP, and (e and f) Ni/NiS-3@CP samples prepared by single step electrodeposition process.

dispersed cauliflower-like nanostructure over the CP support with an average size of 80–100 nm, indicating completely coating of the CP by the deposited catalyst, as drawn in Fig. 3c–f. The coatings exhibit a cauliflower or broccoli-like surface morphology even at lower Ni concentrations (Fig. 3c). From Fig. 3e and f we can infer that the Ni/NiS-3@CP sample can completely cover the surface of the CP substrate forming a denser film due to its higher deposited mass (2.0 mg cm^{-2}) compared with other materials previously mentioned. More-over, Fig. S2† displays the EDS elemental analysis using the related SEM images for the Ni/NiS-3 film. The EDS spectrum confirms the presence of Ni, C, O and S at an atomic ratio of 36.10, 35.34, 25.64, 2.92 at%.

Furthermore, Fig. 4a–d displays the HR-TEM images of the as-made Ni/NiS-3@CP catalyst in which a mixture of crystalline

and amorphous regions was precisely measured. The clear lattice fringe with interplanar d-spacing of 0.299 nm in the crystalline region was assigned to the (100) plane of Ni/NiS-3@CP, attributing to the formation of hybrid nickel sulfide. The SEM, EDS, and HR-TEM results are well in agreement with that previously confirmed by XRD and Raman analysis.

The XPS analysis was probed to further provide the element composition and the surface chemical state of the electro-deposited Ni/NiS-3@CP film. Fig. 5a (wide scan) indicated the presence of C, O, Ni and S peaks, which was approximately in agreement with the EDS analysis (Table S1†). Other peaks in the XPS survey could have been caused by surface species on the electrode. These peaks are likely caused by residual solvents, adventitious carbon, and oxide formation on NiS surfaces. In these electrodes, there is a rather high oxygen content, which
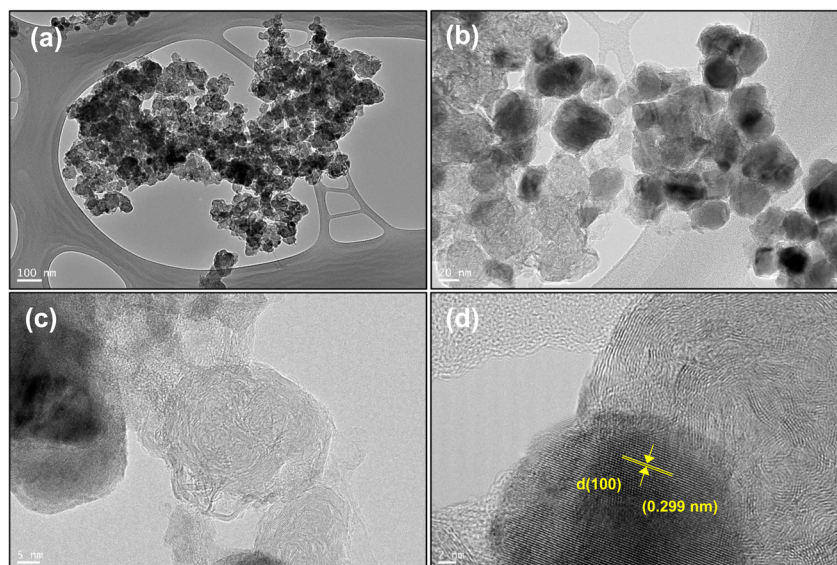

Fig. 4 TEM photographs of fabricated optimal Ni/NiS-3@CP electrodes at dissimilar magnifications (a–d).
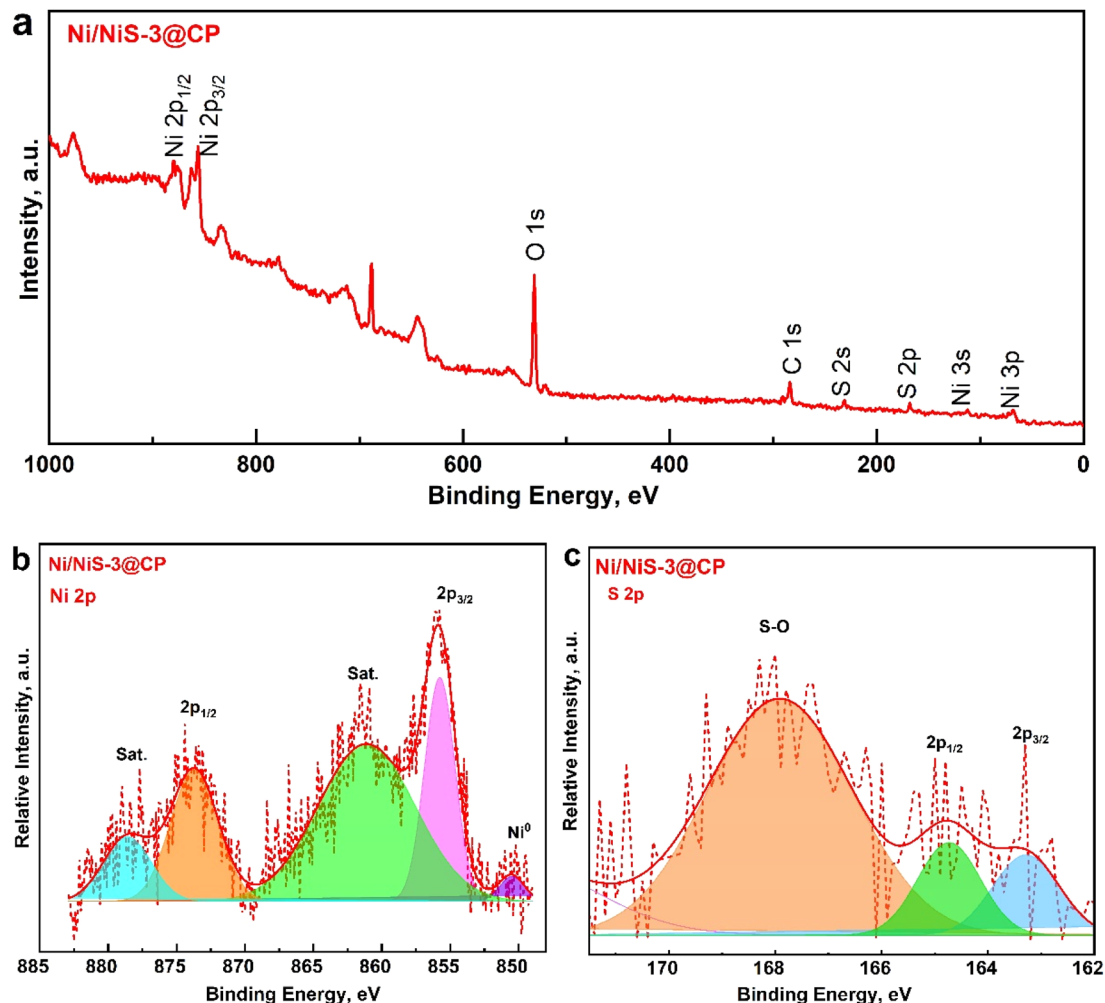
Fig. 5 Surface and chemical features of electrodes (a) XPS survey spectrum for the synthesized Ni/NiS-3@CP, (b and c) high-resolution XPS spectra for Ni 2p and S 2p correspondingly.

might be the result of surface oxidation of NiS.[36] The Ni and S elements were individually scanned to show the uniform distribution on the CP surface. Besides, it was also observed the existence of O species in the survey spectra supports the EDS analysis, which may attribute to the oxygen-containing in an electrolyte bath and surface oxidation during the preparation.[20,37] As seen in Fig. 5b, the high-resolution Ni 2p spectrum can be fitted with two spin–orbit doublets centered at 855.8 and 873.9 eV assigning to Ni $2p_{3/2}$ and Ni $2p_{1/2}$ lattice Ni^{3+}, respectively, and two shark-up satellites marked as "Sat".[38] An additional peak is observed at 850.3 eV, associated with metallic Ni on the exposed CP film.[39] XPS results further confirm the coexistence of Ni and NiS phases, highlighting the metallic nature of Ni in the composite material. For the high-resolution S 2p spectrum of the Ni/NiS-3@CP electrode (Fig. 5c), the peaks appeared at binding energy 163.3 and 164.7 eV correspond to the typical metal–sulfur bonds, confirming the presence of S element as a sulfur anion in the NiS lattice.[40] While, the peak at 167.9 eV is assigned to oxidized S species formed on the surface of Ni/NiS-3@CP due to the exposure of the sample to air.[25]

3.2. Electrochemical measurements of Ni/NiS catalyst

The electrocatalytic performance of unmodified CP, nickel-deposited CP, and varied Ni/NiS@CP compositional catalysts toward UORs was comprehensively evaluated through cyclic voltammetry (CV), constant current/voltage analyses, and electrochemical impedance spectroscopy (EIS) under systematically modulated experimental conditions. The electrocatalytic behavior of a series of as-deposited Ni/NiS@CP (0.5×1.0 cm^{-2}) electrodes for the UOR was carried out in 1.0 M KOH and 0.33 M urea per KOH (Fig. 6a). Clearly, the as-prepared Ni/NiS@CP and bare Ni@CP electrocatalysts exhibit characteristic redox transformation peaks related to the Ni(II)/Ni(III) species about 1.45 V vs. RHE.[41,42] An upsurge in cathodic current density with increasing the Ni content is associated with the characteristic reduction peak of NiOOH species. However, with the introduction of 0.33 M urea, the Ni/NiS-3/CP electrode exhibits better performance for UOR, where the anodic current density can reach up to 75.1 mA cm^{-2} at 1.60 V, whereas only smaller anodic currents are recorded over the bare Ni/CP (27.6 mA cm^{-2}), implying that the Ni/NiS-3@CP electrode has more active sites
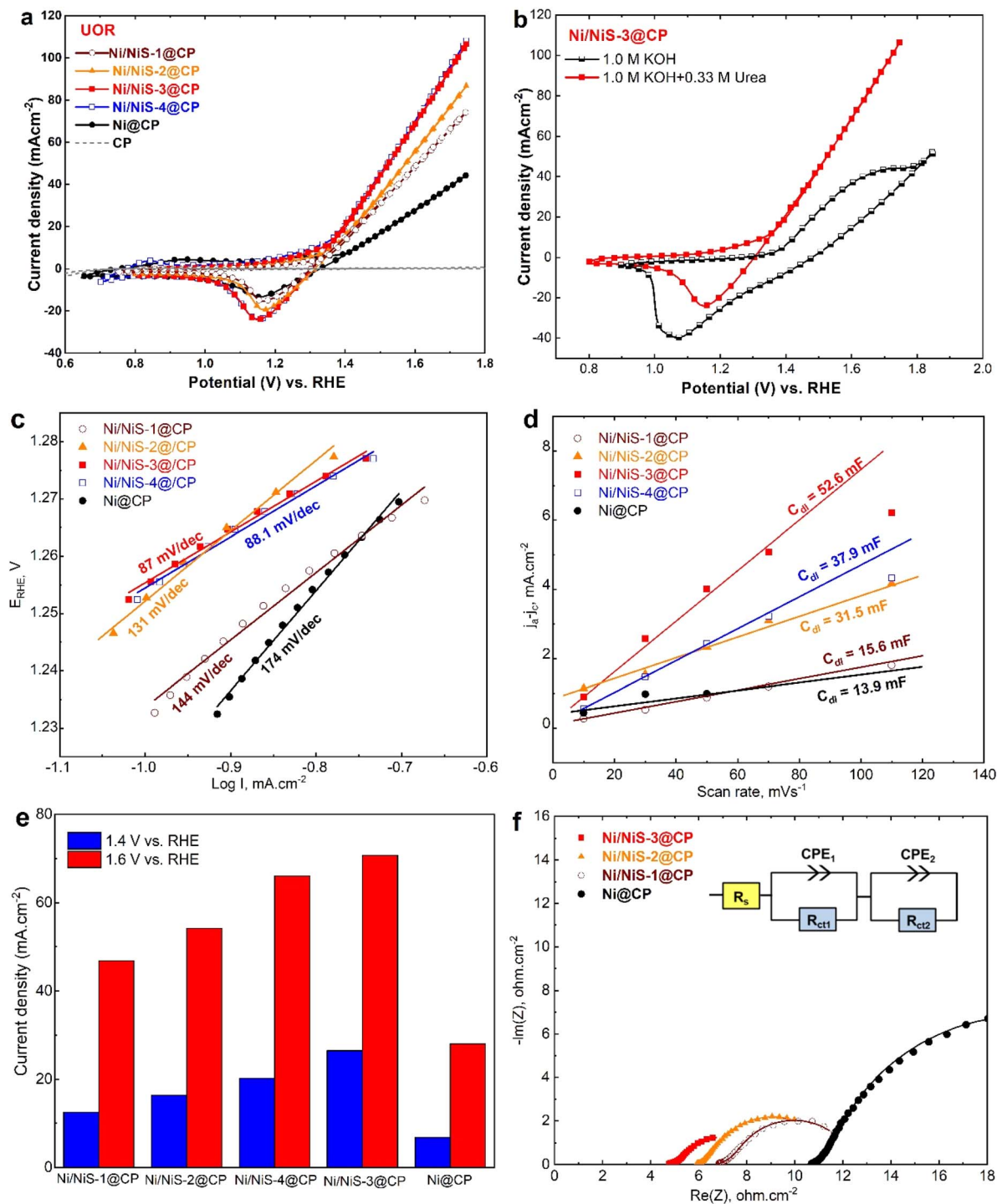
Fig. 6 Electrochemical analysis for UOR. (a) Cyclic voltammetric plots of bare Ni@CP and different ratios of Ni/NiS-x@CP films at 50 mV s^{-1} in 1.0 M KOH/0.33 M urea (b), CV of Ni/NiS-3@CP electrodes under the presence and absence of 0.33 M urea at 50 mV s^{-1}, (c) corresponded Tafel plots of obtained catalysts for UOR (d), double layers capacitances of as-deposited Ni@CP and different ratios of Ni/NiS-x@CP electrocatalysts plotted vs. different scan rates (e), the current density of Ni@CP and different ratios of Ni/NiS-x@CP electrocatalysts at 1.4 and 1.6 V vs. RHE (f), EIS nyquist plots of Ni@CP and different ratios of Ni/NiS-x@CP electrodes at 1.55 V vs. RHE.

than other electrodes, as drawn in Fig. 6b. Notably, the Ni/NiS-3@CP electrode displays a comparable anodic current density to the Ni/NiS-4@CP electrode for the alkaline UOR process, indicating no more enhancement for alkaline UOR as the nickel

amount in various ratios of Ni/N$_i$S@CP exceeds 0.065 M for heterostructure electrodes. Furthermore, the overpotential (η) at 10 mA cm^{-2} are just 1.36, 1.36, 1.35, 1.35, and 1.40 V vs. RHE for Ni/NiS-1@CP, Ni/NiS-2@CP, Ni/NiS-3/CP, Ni/NiS-4@CP, and

bare Ni@CP, respectively. Notably, the Ni/NiS-4@CP displays relatively lower oxygen evolution performance with a high overpotential of 1.80 V vs. RHE in 1.0 M KOH at 50 mA cm^{-2} (Fig. 6b), however, after the introduction of 0.33 M urea, the onset potential is lowered to 1.36 V vs. RHE, indicating that the electrocatalytic of UOR is more energetically favorable than the water oxidation reaction in alkaline conditions. Additionally, an increase in the anodic current density in 0.33 M urea solution has occurred at the same onset potential (1.35 V$_{RHE}$) where the NiOOH is formed, confirming that NiOOH is the active form for UOR. Notably, compared with most of the heterostructure Ni/NiS-based catalysts reported in the alkaline solution literature, our NiNiS-3@CP material has superior UOR, as shown in Table 1. To further investigate the UOR kinetics on the electrodeposited electrodes, the Tafel plots analysis for all samples in the presence of 0.33 M urea at 50 mV s^{-1} was employed, as seen in Fig. 6c. It was estimated by fitting the Tafel equation to the linear region of Fig. 6a for all catalysts: Ni/NiS-1@CP, Ni/NiS-2@CP, Ni/NiS-3@CP, Ni/NiS-4@CP, and Ni@CP, which are 144, 131, 87.7, 88.1, and 174 mV dec^{-1}, respectively. Comparatively, the results confirmed that the Ni/NiS-3@CP (87.7 mV dec^{-1}) film had a much lower Tafel slope than that of bare Ni@CP (174 mV dec^{-1}), indicating that the UOR kinetic and a superior UOR catalytic performance could be quicker over the Ni/NiS-3@CP surface.

Generally, the intrinsic electrocatalytic performance of synthesized electrocatalysts displays a direct correlation with their electrochemically accessible surface area (ECSA). Significantly, the electrochemical double-layer capacitance (C_{dl}), derived from voltammetric measurements, serves as a quantitative metric directly proportional to the electrode's surface area accessibility. Fig. 6d exhibits the electrochemical C_{dl} of as-deposited Ni$_x$S/CP films in the potential range of -0.05 to -0.15 V in 1.0 M KOH at different sweep rates from 10–110 mV s^{-1}. The average values of anodic and cathodic current (j_a–j_c) of the obtained catalysts were plotted in Fig. 6d. The C_{dl} values of the as-made films Ni/NiS-1@CP, Ni/NiS-2@CP, Ni/NiS-3@CP, Ni/NiS-4@CP, and Ni@CP were found to be 15.6, 31.5, 52.6, 37.9, and 13.9 mF, respectively, confirming that the more active sites exposure for Ni/NiS-3@CP than other ratios of

Ni/NiS@CP and bare Ni@CP. Conventionally, the specific capacitance (C_s) for a standardized 1 cm^2 planar surface is approximated at 40 μF cm^{-2}. The ECSA can be quantitatively determined through the mathematical relationship: ECSA = C_{dl}/C_s, where C_{dl} represents the measured double-layer capacitance. Also, the ECSA values for Ni@CP, Ni/NiS-1@CP, Ni/NiS-2@CP, Ni/NiS-3@CP and Ni/NiS-4@CP were 348 cm^2, 390 cm^2, 788 cm^2, 1315 cm^2 and 948 cm^2, respectively indicates that the more active sites significantly resulted from the Ni/NiS-3 film deposited over CP (Fig. 6d and S6†). The ECSA is primarily influenced by the surface roughness, the surface exposure, and the conductivity of the electrodes. As mentioned earlier in Fig. 6a, the Ni/NiS-3@/CP catalyst clearly reveals a higher anodic current density in 0.33 M urea at 1.6 V vs. RHE, which was 2.5 times than bare Ni@CP catalyst, supporting the significance conductivity enhancement. For comparison, Fig. 6e presents the peak current density of as-prepared catalysts at 1.4 and 1.6 V$_{RHE}$. Certainly, the larger current density of Ni/NiS-3@CP electrode can reach ca. 75.1 mA cm^{-2} at 1.6 V$_{RHE}$, which was greater than bare Ni@CP catalyst (27.6 mA cm^{-2}). Evidently, the Ni/NiS-3@CP catalyst shows the lowest Tafel slope and highest C_{dl}, which further accounts for its best UOR performance among them. The EIS analysis were also executed for the alkaline UOR at 1.35 V at all the studied materials, as shown in Fig. 6f. The radii of the arc obtained for all materials followed the order as bare Ni@CP > Ni/NiS-1@CP > Ni/NiS-2@CP > Ni/NiS-3@CP electrodes. The EIS measurements were also fitted via a typical equivalent circuit (inset in Fig. 6f) similar to those mentioned in the literature associated with alkaline urea oxidation reaction.[42,43] The circuit consists of a parallel combination of the contact resistance (R_o) between the CP support and the catalyst material, and the constant phase element, CPE (R_o, CPE$_1$), and charge transfer resistance arising from the electrocatalytic UOR, R_{ct} (R_{ct}, CPE$_2$) element in series with solution resistance of R_s. The CPE refers to the double layer capacitor at the electrode/electrolyte interface and is generally employed to replace the pure capacitor according to its physical basis relating to the CPE to the frequency distribution of the capacitance.[11,41] The fitted EIS parameters were reported in Table S2.† By comparing the R_{ct} values of all the evaluated

Table 1 Comparison of the UOR performance of several previously reported active nickel sulfide catalysts supported on different substrates in alkaline medium

Catalysts	η_{10}, V	Current density at 1.6 V, mA cm^{-2}	Tafel slope, mV dec^{-1}	ECSA, mF	Substrate	Ref.
Ni/NiS-3@CP	1.35	75.1	88.1	52.6	CP	This work
Ni/NiS-2@CP	1.36	46.7	144	15.62	CP	This work
Bare Ni@CP	1.40	27.6	174	13.94	CP	This work
β-NiS nanoflower	1.40	100	66	1.92	NF	25
MoS$_2$/Ni$_3$S$_2$/Ni/NF	1.33	~700	42	64.4	NF	26
Ni$_3$S$_2$ nanowires	1.30	400	46	—	NF	27
N-NiS/NiS$_2$	1.33	~140	28.34	5.8	CP	28
NiSe$_2$ nanoflakes	1.324	~110	20	5	NF	44
CoS/Ni$_3$S$_2$@CP	1.32	72	206	17.81	CP	45
Ni@C-V$_2$O$_3$/NF	1.36	~100	59.52	—	NF	46
Co$_2$P–Ni$_3$S$_2$	1.338	~100	54.52	—	GCE	47

samples, the Ni/NiS-3@CP catalyst had the smallest R_{ct} value (1.424 ohm), confirming its highest catalytic activity for UOR performance in 1.0 M KOH. To further probe the excellent electrocatalytic performance of Ni/NiS-3@CP catalyst for the UOR in 1.0 M KOH containing 0.33 M urea solution, Nyquist plot at different potentials was also performed. Fig. S3† shows the Nyquist plot for urea oxidation reaction in an alkaline environment at Ni/NiS-3@CP at varied potentials. Clearly, it was observed that the semicircle diameter decreases as the anodic oxidation potential was displaced from 1.35 to 1.55 V *vs.* RHE, indicating urea oxidation reaction at Ni/NiS-3@CP catalyst is considerably improved at a higher potential of 1.55 V_{RHE}, that agrees with the CVs results (Fig. 6a).

To further assess the electrochemical stability of the obtained Ni/NiS@CP electrodes for alkaline UOR, the CA measurements at a constant potential of 1.55 V *vs.* RHE for about 18 h in 0.33 M urea per KOH were carried out. As shown

in Fig. 7a, generally, a stable current remains through a measurement time of about 18 h in 0.33 M urea per KOH without any decay. Moreover, the Ni/NiS-3@CP material clearly displays a superior current density than that of bare Ni@CP and other different ratios of Ni/NiS@CP, evaluating the high electroactivity performance and exceptional durability for UOR at this catalyst, consisting with the voltammetric results (Fig. 6a). Importantly, the above electrochemical measurements confirm that the Ni/NiS-3@CP have superior activity and excellent durability for alkaline UOR compared with bare Ni@CP under the same condition, indicating the presence of heteroatom of sulfur led to a variety in the active sites and resulting in highly enhancement during UOR process. The structure and composition of Ni/NiS-3@CP after the test were also analyzed synthetically using XRD, Raman spectra and FE-SEM. Furthermore, the XRD (Fig. 7b) and Raman spectra (Fig. 7c) of the Ni/NiS-3@CP reveal a slight crystallinity change after *i–t*
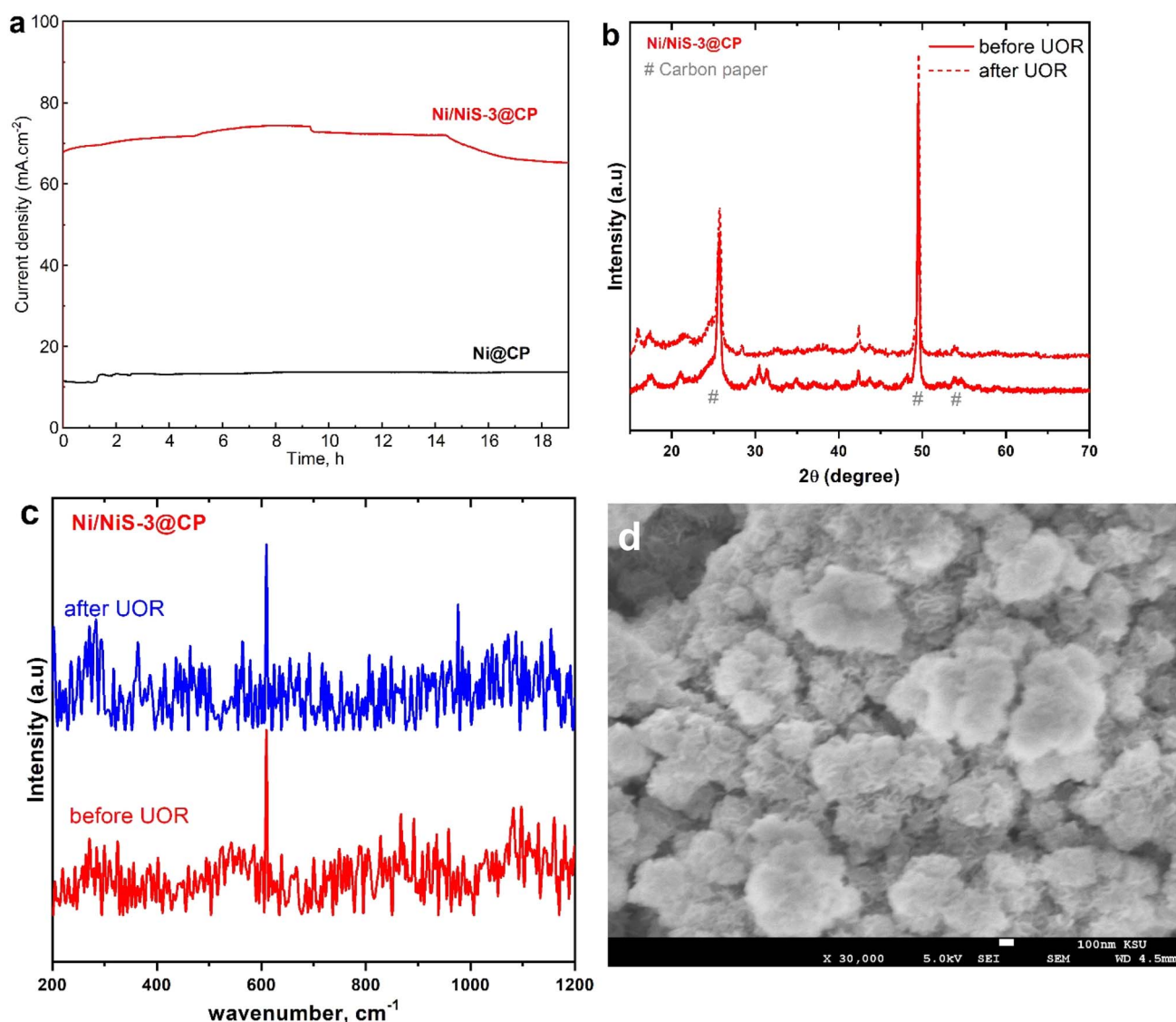

Fig. 7 Durability tests. (a) Time-dependent current density curves for Ni/NiS-*x*@CP under a constant potential in 1 M KOH/0.33 M urea solution. (b) XRD, (c) Raman, and (d) FE-SEM imaged of Ni/NiS-3@CP electrodes before and after durability tests.

measurements, verifying the phase stability. More importantly, FE-SEM images of Ni/NiS-3@CP electrocatalysts were attained at 19 h to inspect the mass loss of electrodes during the UORs (Fig. 7d). This electrode material was found to be more durable than other UOR electrocatalysts examined. In an alkaline medium, the Ni/NiS-3@CP electrocatalyst exhibits extremely high UOR activity and excellent stability.

3.3. HER performance of Ni/NiS electrodes

The electrochemical behavior of the different as-deposited Ni/NiS electrodes was also tested for HER in an acidic medium of 0.5 M H_2SO_4 at 5 mV s^{-1} using a typical three-electrode setup. Fig. 8a exhibits the linear sweep voltammetry (LSV) of the obtained catalysts, the CP support, and a commercial Pt/C@CP (10%). The LSV curves point out the CP support shows no HER response; meanwhile, as-deposited Ni/NiS-3/CP electrode displays a significant enhancement in the cathodic current density compared with other ratios of Ni/NiS-1@CP, Ni/NiS-2@CP and bare Ni@CP electrodes. Obviously, the Ni/NiS-

3@CP catalysts reveal an overpotential of 125 mV at 10 mA cm^{-2}, which is apparently lower than bare Ni@CP (397 mV), Ni/NiS-1@CP (266 mV) and Ni/NiS-2@CP (260 mV), confirming that the Ni/NiS-3@CP catalyst has more excellent activity for HER. Additionally, the corresponding Tafel slope of as-prepared Ni/NiS-3@CP, Ni/NiS-2@CP, Ni/NiS-1@CP, and bare Ni@CP were found to be 180, 231, 328, and 343 mV dec^{-1}, respectively, as shown in Fig. 8b. The lower Tafel slope of Ni/NiS-3@CP electrode confirms a Volmer mechanism and illustrates the faster HER kinetic due to its higher exposure active sites, which is also confirmed by the EIS measurements in Fig. 8c. Tafel slopes for Ni/NiS-3@CP in an acidic medium indicate that HER is processed through the Heyrovsky mechanism.[48] Thus, smaller Tafel values suggest more efficient kinetics and greater electrocatalytic properties of Ni/NiS-3@CP towards HER. Nyquist plots of the obtained catalysts in 0.5 M H_2SO_4 at −0.223 V vs. RHE indicate that the Ni/NiS-3@CP electrode has the lower charge transfer resistance ($R_2 = 5.525$ ohm) than bare Ni@CP electrode (385.8 ohm) (ESI, Table S3†), demonstrating
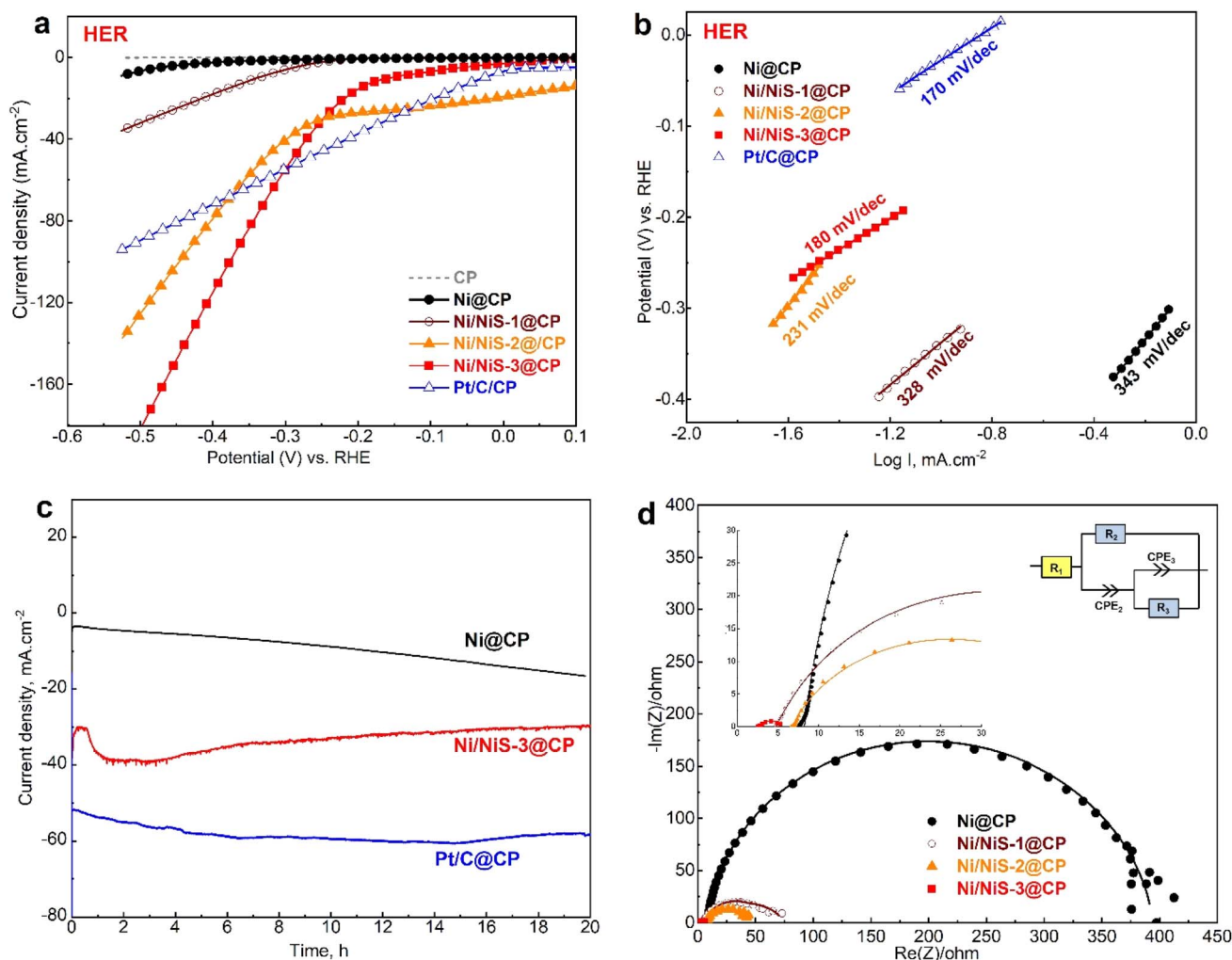

Fig. 8 (a) Polarization curves of the fabricated Ni@CP and different Ni/NiS@CP electrodes and the benchmark Pt/C for HER, (b) corresponding Tafel slope, (c) chronoamperometric curves for Ni@CP, Ni/NiS-3@CP electrodes, and Pt/C electrodes for HER. (d) Nyquist plots of fabricated samples evaluated on a CP electrode at −0.300 V_{RHE} for HER catalysis.

more efficient catalytic HER kinetic. The CA was also carried out to further confirm the HER activity of the obtained electrodes. Fig. 8d shows the long-term stability of the Ni/NiS-3@CP electrode in 0.5 M H_2SO_4 at −0.273 V *vs.* RHE, in which the Ni/NiS-3@CP catalyst well maintains the current density unchanged for 20 h after running the HER. The overall results confirm that the Ni/NiS-3@CP electrode shows the best performance toward HER, consistent with that previously mentioned in CV analysis.

4 Conclusion

In summary, a bifunctional heterostructured Ni/NiS catalyst supported on CP toward UOR and HER was successfully fabricated by a facile, easily scalable, and cost-efficient thiourea-assisted electrodeposition process. These Ni/NiS@CP catalysts had high surface area (ECSA), strong charge transfer capability, excellent electrochemical activity, high stability, synergistic effects, and gas production efficiency. Impressively, the as-prepared Ni/NiS@CP films displays improved electrocatalytic activity toward UOR, especially delivering a low overpotential of 1.75 V at 100 mA cm^{-2} in basic medium. As well, it requires a low overpotential of 125 mV at 10 mA cm^{-2} during the HER process. In this study, electrodeposited Ni/NiS over CP enhances the catalytic activity of the UOR and the HER by a synergistic effect. In this study, we present a promising avenue for developing effective catalysts for hydrogen production systems that are fueled by energy-efficient organic molecules.

Data availability

The data supporting this article have been included as part of the ESI.†

Author contributions

Saba A. Aladeemy: data curation, formal analysis, investigation, writing – original draft. Prabhakarn Arunachalam: conceptualization, writing – review & editing, data curation, supervision. Mabrook S. Amer: data curation, formal analysis, Abdullah M. Al-Mayouf: supervision, funding acquisition, project administration.

Conflicts of interest

The authors declare that they have no known competing financial interests or personal relationships that could have appeared to influence the work reported in this paper.

Acknowledgements

References

1 J. Wang, X. Yue, Y. Yang, S. Sirisomboonchai, P. Wang, X. Ma, A. Abudula and G. Guan, *J. Alloys Compd.*, 2020, **819**, 1–23.

2 S. Anantharaj, S. R. Ede, K. Sakthikumar, K. Karthick, S. Mishra and S. Kundu, *ACS Catal.*, 2016, **6**, 8069–8097.

3 J. Joy, J. Mathew and S. C. George, *Int. J. Hydrogen Energy*, 2018, **43**, 4804–4817.

4 J. Wang, W. Cui, Q. Liu, Z. Xing, A. M. Asiri and X. Sun, *Adv. Mater.*, 2016, **28**, 215–230.

5 R. Lan and S. Tao, *J. Power Sources*, 2011, **196**, 5021–5026.

6 X. Li, X. Hao, G. Guan, A. Abudula and G. Guan, *J. Mater. Chem. A*, 2016, **4**, 11973–12000.

7 D. Zhu, C. Guo, J. Liu, L. Wang, Y. Du and S. Z. Qiao, *Chem. Commun.*, 2017, **53**, 10906–10909.

8 G. Wang and Z. Wen, *Nanoscale*, 2018, **10**, 21087–21095.

9 S. Wei, X. Wang, J. Wang, X. Sun, L. Cui, W. Yang, Y. Zheng and J. Liu, *Electrochim. Acta*, 2017, **246**, 776–782.

10 P. Basumatary, D. Konwar and Y. S. Yoon, *Electrochim. Acta*, 2018, **261**, 78–85.

11 S. A. Aladeemy, A. Al-Mayouf, M. Amer, N. Alotaibi, M. T. Weller and M. A. Ghanem, *RSC Adv.*, 2021, 3190–3201.

12 S. A. Aladeemy, A. M. Al-Mayouf, M. N. Shaddad, M. S. Amer, N. K. Almutairi, M. A. Ghanem, N. H. Alotaibi and P. Arunachalam, *Catalysts*, 2021, **11**, 102.

13 L. Wang, T. Du, J. Cheng, X. Xie, B. Yang and M. Li, *J. Power Sources*, 2015, **280**, 550–554.

14 R. Lan, S. Tao and J. T. S. Irvine, *Energy Environ. Sci.*, 2010, **3**, 438–441.

15 J. Tian, Q. Liu, A. M. Asiri and X. Sun, *J. Am. Chem. Soc.*, 2014, 14–17.

16 Y. Lee, J. Suntivich, K. J. May, E. E. Perry and Y. Shao-Horn, *J. Phys. Chem. Lett.*, 2012, **3**, 399–404.

17 K. Ye, G. Wang, D. Cao and G. Wang, *Top. Curr. Chem.*, 2018, **376**, 41–78.

18 W. Xu, Z. Wu and S. Tao, *Energy Technol.*, 2016, **4**, 1–10.

19 X. Hu, J. Zhu, J. Li and Q. Wu, *ChemElectroChem*, 2020, **7**, 3211–3228.

20 L. Wang, W. Liu, T. Sangeetha, Z. Guo, Z. He, C. Chen, L. Gao and A. Wang, *Int. J. Hydrogen Energy*, 2020, **45**, 6583–6591.

21 A. Irshad and N. Munichandraiah, *ACS Appl. Mater. Interfaces.*, 2017, **9**, 19746–19755.

22 N. Jiang, L. Bogoev, M. Popova, S. Gul, J. Yano and S. Yujie, *J. Mater. Chem. A*, 2014, **2**, 19407–19414.

23 T. Tian, L. Huang, L. Ai and J. Jiang, *J. Mater. Chem. A*, 2017, **5**, 20985–20992.

24 G. Ren, Q. Hao, J. Mao, L. Liang, H. Liu, C. Liu and J. Zhang, *Nanoscale*, 2018, **10**, 17347–17353.

25 T. H. Wu, Y. C. Lin, B. W. Hou and W. Y. Liang, *Catalysts*, 2020, **10**, 1–11.

26 F. Li, J. Cheng, D. Zhang, W.-F. Fu, Y. Chen, Z. Wen and X.-J. Lv, *Chem. Commun.*, 2018, **54**, 5181–5184.

27 M. Liu, Y. Jiao, S. Zhan and H. Wang, *Catal. Today*, 2019, **355**, 596–601.

28 H. Liu, Z. Liu, F. Wang and L. Feng, *Chem. Eng. J.*, 2020, **397**, 125507–125516.

29 N. Jiang, Q. Tang, M. Sheng, B. You, D. E. Jiang and Y. Sun, *Catal. Sci. Technol.*, 2016, **6**, 1077–1084.

30 L. L. Feng, G. Yu, Y. Wu, G. D. Li, H. Li, Y. Sun, T. Asefa, W. Chen and X. Zou, *J. Am. Chem. Soc.*, 2015, **137**, 14023–14026.

31 A. Cuña, C. R. Plascencia, E. L. da Silva, J. Marcuzzo, S. Khan, N. Tancredi, M. R. Baldan and C. de Fraga Malfatti, *Appl. Catal. B: Environ.*, 2017, **202**, 95–103.

32 A. K. Singh, N. Yasri, K. Karan and E. P. L. Roberts, *ACS Appl. Energy Mater.*, 2019, **2**, 2324–2336.

33 J. Y. Lin, J. H. Liao and S. W. Chou, *Electrochim. Acta*, 2011, **56**, 8818–8826.

34 J. Zhang, Y. Wang, J. Cui, J. Wu, X. Shu, C. Yu, H. Bai, M. Zhai, Y. Qin, H. Zheng, *et al.*, *Int. J. Hydrogen Energy*, 2018, **43**, 16061–16067.

35 R. Li, P. Kuang, L. Wang, H. Tang and J. Yu, *Chem. Eng. J.*, 2021, 134137.

36 J. Lv, Y. Cheng, W. Liu, B. Quan, X. Liang, G. Ji and Y. Du, *J. Mater. Chem. C*, 2018, **6**, 1822–1828.

37 R. Levinas, N. Tsyntsaru and H. Cesiulis, *Catalysts*, 2020, **10**, 1182.

38 Y. Ji, W. Liu, Z. Zhang, Y. Wang, X. Zhao, B. Li, X. Wang, B. Liu and S. Feng, *RSC Adv.*, 2017, **7**, 44289–44295.

39 G. Liu, C. Shuai, Z. Mo, R. Guo, N. Liu, X. Niu, Q. Dong, J. Wang, Q. Gao, Y. Chen and W. Liu, *New J. Chem.*, 2020, **44**, 17313.

40 B. Guan, Y. Li, B. Yin, K. Liu, D. Wang, H. Zhang and C. Cheng, *Chem. Eng. J.*, 2017, **308**, 1165–1173.

41 D. Yang, L. Yang, L. Zhong, X. Yu and L. Feng, *Electrochim. Acta*, 2019, **295**, 524–531.

42 R. K. Singh, P. Subramanian and A. Schechter, *ChemElectroChem*, 2017, **4**, 1037–1043.

43 M. S. Amer, P. Arunachalam, A. M. Alsalman, A. M. Al-Mayouf, Z. A. Almutairi, S. A. Aladeemy and M. Hezam, *Catal. Today*, 2022, **397–399**, 197–205.

44 J. Sun, X. Hu, Z. Huang, T. Huang, X. Wang, H. Guo, F. Dai and D. Sun, *Nano Res.*, 2020, **13**, 2056–2062.

45 S. A. Aladeemy, P. Arunachalam, A. M. Al-Mayouf, P. N. Sudha, A. Rekha, A. Vidhya, J. Hemapriya, S. Latha, P. S. Prasad, S. Pavithra, *et al.*, *Catalysts*, 2024, **14**, 570.

46 G. Qian, J. Chen, L. Luo, H. Zhang, W. Chen, Z. Gao, S. Yin and P. Tsiakaras, *ACS Appl. Mater. Interfaces*, 2020, **12**, 38061–38069.

47 T. Chen, Q. Wu, F. Li, R. Zhong and Z. Chen, *ACS Appl. Nano Mater.*, 2023, **6**, 18364–18371.

48 P. Liu, J. Zhu, J. Zhang, P. Xi, K. Tao, D. Gao and D. Xue, *ACS Energy Lett.*, 2017, **2**, 745–752.